Optimal slip velocities of micro-swimmers with arbitrary axisymmetric shapes

Hanliang Guo[1], Hai Zhu[1], Ruowen Liu[1], Marc Bonnet[2], and Shravan Veerapaneni[1]†

[1]Department of Mathematics, University of Michigan, Ann Arbor, MI, 48109 USA.
[2]POEMS (CNRS, INRIA, ENSTA), ENSTA Paris, 91120 Palaiseau, France.

(Received xx; revised xx; accepted xx)

This article presents a computational approach for determining the optimal slip velocities on any given shape of an axisymmetric micro-swimmer suspended in a viscous fluid. The objective is to minimize the power loss to maintain a target swimming speed, or equivalently to maximize the efficiency of the micro-swimmer. Owing to the linearity of the Stokes equations governing the fluid motion, we show that this PDE-constrained optimization problem can be reduced to a simpler quadratic optimization problem, which we solve using a high-order accurate boundary integral method. We consider various families of shapes parameterized by the reduced volume and compute their swimming efficiency. We found that for a given reduced volume, prolate ellipsoids are the most efficient micro-swimmer shapes and that, irrespective of the shape, the optimal slip always corresponds to a neutral swimmer (as opposed to a pusher or a puller).

1. Introduction

The *squirmer model* (Lighthill 1952; Blake 1971) is widely adopted by mathematicians and physicists over the past decades to model ciliated micro-swimmers such as *Opalina*, *Volvox* and *Paramecium* (Lauga & Powers 2009). On a high level, this continuum model, sometimes referred to as the *envelope model*, effectively tracks the motion of the envelope formed by the tips of the densely-packed cilia, located on the swimmer body, while neglecting the motion below the tips. Individual and collective ciliary motions could be mapped to traveling waves of the envelope on the surface. Assuming no radial displacements of the surface and time-independent tangential velocity led to the simpler *steady* squirmer model (see Pedley 2016), wherein, a prescribed slip velocity on the boundary propels the squirmer. While the model was originally designed for spherical shapes, it has since been adapted to more general shapes and has recently been shown to capture realistic collective behavior of suspensions (Kyoya *et al.* 2015).

Shape is also a key parameter in the design of artificial micro-swimmers in applications such as targeted drug delivery. In particular, the squirmer model is often employed to study the propulsion of *phoretic particles*, which are micro- to nano-meter sized particles that propel themselves by exploiting the asymmetry of chemical reactions on their surfaces (Anderson 1989; Golestanian *et al.* 2007). A classical example is the Janus sphere (Howse *et al.* 2007), which consists of inert and catalytic hemispheres. When submerged in a suitable chemical solution, the asymmetry between the chemical reactions on the two hemispheres creates a concentration gradient. The gradient creates an effective steady slip velocity on the surface via osmosis that naturally suits the squirmer model. Besides the classical Janus spheres and bi-metallic nanorods (Paxton *et al.* 2004), more

† Email address for correspondence: shravan@umich.edu

sophisticated shapes have also been proposed recently, such as two-spheres (Valadares *et al.* 2010; Palacci *et al.* 2015), spherocylinder (Uspal *et al.* 2018), matchsticks (Morgan *et al.* 2014) and microstars (Simmchen *et al.* 2017). Interestingly, Uspal *et al.* (2018) showed that special shapes of phoretic particles exhibit novel properties such as 'edge-following' when put close to chemically patterned surfaces.

Studying the efficiency of biological micro-swimmers is pivotal to understanding natural systems and designing artificial ones for accomplishing various physical tasks. The mechanical efficiency (Lighthill 1975) of the spherical squirmer can be directly computed, as its rate of viscous energy dissipation, or power loss, can be written in terms of the modes of the squirming motion. Michelin & Lauga (2010) found the optimal swimming strokes of unsteady spherical squirmers by employing a pseudo-spectral method for solving the Stokes equations that govern the ambient fluid and a numerical optimization procedure. Their approach, however, does not readily generalize to arbitrary shapes. On the other hand, Leshansky *et al.* (2007) analytically investigated the efficiency of micro-swimmers of prolate ellipsoidal shapes with a time-independent 'treadmilling' slip velocity and found that the efficiency increases unboundedly with the aspect ratio. Vilfan (2012) optimized the steady slip velocity and the shape at the same time, with constraints on its volume and maximum curvature. However, this work was restricted to the case where the power loss at each point is solely based on the *local* slip velocity, uncoupled from its neighboring points (e.g., when cilia are far apart).

In this note, we address the following broader question: *Given an axisymmetric shape of a steady squirmer, what is the slip velocity that maximizes its swimming efficiency?* The optimization problem, being quadratic, is reduced to a linear system of equations solved by a direct method, while forward exterior flow problems are solved using a boundary integral method. Those combined features produce a simple and efficient solution procedure. We introduce the optimization problem and our numerical solver in Section 2, present the optimal solution for various shape families in Section 3, followed by conclusions and a discussion on future research directions in Section 4.

2. Problem Formulation and Numerical Solution

2.1. *Model*

Consider an axisymmetric micro-swimmer whose boundary Γ can be obtained by rotating a curve γ about $\boldsymbol{e}_3$ axis as shown in Fig. 1(a). Using the arc-length $s \in [0, \ell]$ to parameterize the generating curve, its coordinate functions can be written as $\gamma(s) = (x_1(s), 0, x_3(s))$. Here, we restrict our attention to shapes of spherical topology, therefore, all shapes considered satisfy the conditions $x_1(0) = x_1(\ell) = 0$ and $x_1(s) > 0,\ \forall\, s \in (0, \ell)$. We assume that the micro-swimmer is suspended in an unbounded viscous fluid domain. The governing equations for the ambient fluid in the vanishing Reynolds number limit are given by the Stokes equations:

$$-\mu \nabla^2 \boldsymbol{u} + \nabla p = \boldsymbol{0}, \quad \nabla \cdot \boldsymbol{u} = 0, \tag{2.1}$$

where μ is the fluid viscosity, p and $\boldsymbol{u}$ are the pressure and flow field respectively. In the absence of external forces and imposed flow fields, the far-field boundary condition simply is

$$\lim_{\boldsymbol{x} \to \infty} \boldsymbol{u}(\boldsymbol{x}) = \boldsymbol{0}. \tag{2.2}$$

A tangential slip u^{S} defined on γ propels the micro-swimmer forward with a translational velocity U in the $\boldsymbol{e}_3$ direction. Its angular velocity as well as the translational velocities

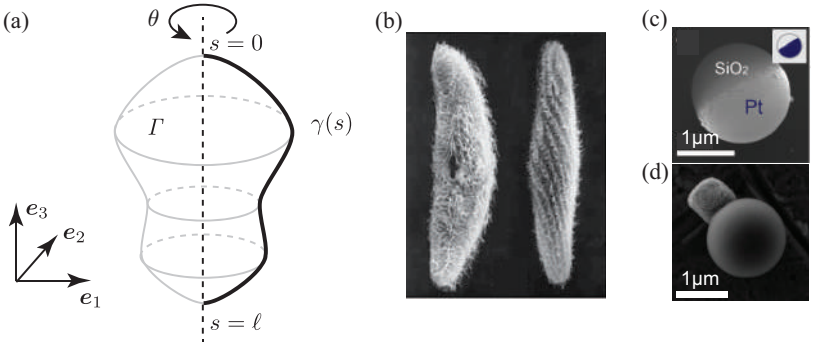

FIGURE 1. (a) Schematic of the micro-swimmer geometry. The shape is assumed to be axisymmetric, obtained by rotating the generating curve γ about the $\boldsymbol{e}_3$ axis. (b) Biological swimmers (Lynn (2008), Chap 4 Fig 4.6). (c) Scanning electron microscope (SEM) image of a single half-coated Janus particle; inset: the dark-blue shows the location of the Pt cap. (Choudhury *et al.* 2017) (d) SEM image of a phototactic swimmer, which consists of a haematite particle extruded from a colloidal bead. (Aubret & Palacci 2018)

in the $\boldsymbol{e}_1$ and $\boldsymbol{e}_2$ directions are zero by symmetry. Consequently, the boundary condition on γ is given by

$$\boldsymbol{u} = u^{\mathrm{S}}\boldsymbol{\tau} + U\boldsymbol{e}_3, \tag{2.3}$$

where $\boldsymbol{\tau}$ is the unit tangent vector on γ. Note that, in order to avoid singularities, the slip must vanish at the end points:

$$u^{\mathrm{S}}(0) = u^{\mathrm{S}}(\ell) = 0. \tag{2.4}$$

Due to the axisymmetry of Γ, the required no-net-torque condition on the freely-suspended microswimmer is automatically satisfied while the no-net-force condition reduces to one scalar equation

$$\int_{\Gamma} \boldsymbol{f}(\boldsymbol{x}) \cdot \boldsymbol{e}_3 \,\mathrm{d}S = 2\pi \int_{\gamma} f_3(\boldsymbol{x})\, x_1 \mathrm{d}s = 0, \tag{2.5}$$

where $\boldsymbol{f}$ is the active force density on the micro-swimmer surface (negative to fluid traction) and f_3 is its $\boldsymbol{e}_3$ component.

We quantify the performance of the micro-swimmer with slip velocity u^{S} by its power loss while maintaining a target swimming speed U. The power loss is defined by

$$P = \int_{\Gamma} \boldsymbol{f} \cdot \boldsymbol{u} \,\mathrm{d}S = 2\pi \int_{\gamma} \boldsymbol{f} \cdot (u^{\mathrm{S}}\boldsymbol{\tau} + U\boldsymbol{e}_3) x_1 \mathrm{d}s. \tag{2.6}$$

Note that P can be made arbitrarily small by lowering the swimming speed U. It is therefore necessary to compare the power loss of different swimmers that have the same swimming speed U. We note that a lower P with a fixed shape and swimming speed U corresponds to a higher efficiency, $\eta = C_D U^2/P$, as defined by Lighthill (1952), where C_D is the drag coefficient of the given swimmer.

2.2. *Boundary integral method for the forward problem*

Before stating the optimization problem, we summarize our numerical solution procedure for (2.1) – (2.3). Again, we fix the swimming speed U, referred to from here onwards as the "target swimming speed", and assume that the tangential slip u^S is given. In general, an arbitrary pair of u^{S} and U does not satisfy the no-net-force condition (2.5). This condition will be treated as a constraint in our optimization problem. Therefore, the

goal is to find the active force density $\boldsymbol{f}$ given the velocity on the boundary γ as in (2.3). We use the single-layer potential ansatz, which expresses the velocity as a convolution of an unknown density function $\boldsymbol{\mu}$ with the Green's function for the Stokes equations G, from which the force density can be determined by convolution with the traction kernel T (Pozrikidis (1992)):

$$\boldsymbol{u}(\boldsymbol{x}) = \int_{\Gamma} G(\boldsymbol{x}-\boldsymbol{y})\,\boldsymbol{\mu}(\boldsymbol{y})\,d\Gamma(\boldsymbol{y}), \quad \boldsymbol{f}(\boldsymbol{x}) = -\int_{\Gamma} T(\boldsymbol{x}-\boldsymbol{y})\cdot\boldsymbol{n}\,\boldsymbol{\mu}(\boldsymbol{y})\,d\Gamma(\boldsymbol{y}), \tag{2.7}$$

where $\boldsymbol{n}$ is the unit normal vector pointing into the fluid. We can solve for $\boldsymbol{\mu}$ by taking the limit of $\boldsymbol{x}\to\Gamma$ in the above ansatz and substituting in (2.3). The boundary integrals in (2.7) become weakly singular on Γ, requiring specialized quadrature rules. Here, we use the approach of Veerapaneni *et al.* (2009) which performs an analytic integration in the $\theta-$direction reducing the integrals to convolutions on the generating curve and applies a high-order quadrature rule designed to handle the $log-$singularity of the resulting kernels.

2.3. *Optimization problem and its reformulation*

The goal is to find a slip profile $u^{\mathrm{S}*}(s)$ that minimizes the power loss P while maintaining the target swimming speed U of a given axisymmetrical micro-swimmer. Let J be the objective function, here equated to P defined in (2.6), and F be the net force functional:

$$J(u^{\mathrm{S}}) := 2\pi\int_{\gamma}\boldsymbol{f}(u^{\mathrm{S}})\cdot(u^{\mathrm{S}}\boldsymbol{\tau}+U\boldsymbol{e}_3)\,x_1\mathrm{d}s, \quad F(u^{\mathrm{S}}) := 2\pi\int_{\gamma}\boldsymbol{f}(u^{\mathrm{S}})\cdot\boldsymbol{e}_3\,x_1\mathrm{d}s. \tag{2.8}$$

They are slip velocity functionals as their values are completely determined by u^{S}. The optimization problem can now be stated as follows:

$$u^{\mathrm{S}*} = \underset{u^{\mathrm{S}}\in\mathcal{U}}{\arg\min}\, J(u^{\mathrm{S}}) \quad \text{subject to } F(u^{\mathrm{S}}) = 0, \tag{2.9}$$

with $\mathcal{U}$ being the space of the all possible slip velocities satisfying (2.4). Notice that the no-net-force condition (2.5) is added as a constraint here.

By (2.3) and linearity of the Stokes equation (2.1), the forward solution $\boldsymbol{u}$ and the net force F are affine in u^{S} ($\boldsymbol{u}$ is linear in u^{S} if $F=0$). Consequently, $J(u^{\mathrm{S}})$ is a quadratic functional and (2.9) is inherently a quadratic optimization problem. To make it more explicit, consider a discretized version of the slip optimization problem where u^{S} is sought in the form

$$u^{\mathrm{S}}(\boldsymbol{x}) = \sum_{k=1}^{m} U\xi_k\, u_k^{\mathrm{S}}(s), \tag{2.10}$$

for some set of m basis functions u_k^{S} satisfying (2.4). We adopt a B-spline formulation for these basis functions (see supplemental material for details). Let $(\boldsymbol{u}_0, p_0, \boldsymbol{f}_0)$ and $(\boldsymbol{u}_k, p_k, \boldsymbol{f}_k)$ (with $1\leqslant k\leqslant m$) denote the solutions of the forward problem (2.1) with $\boldsymbol{u}=\boldsymbol{e}_3$ and $\boldsymbol{u}=u_k^{\mathrm{S}}\boldsymbol{\tau}$ being their boundary conditions on γ, respectively.

The net force $F(u^{\mathrm{S}})$ is then given by $F(u^{\mathrm{S}}) = 2\pi U\mathcal{F}(\boldsymbol{\xi})$, where

$$\mathcal{F}(\boldsymbol{\xi}) := \int_{\gamma}\left(\boldsymbol{f}_0+\sum_{k=1}^{m}\xi_k\boldsymbol{f}_k\right)\cdot\boldsymbol{e}_3\,x_1\mathrm{d}s = F_0+\boldsymbol{F}^{\mathrm{T}}\boldsymbol{\xi}. \tag{2.11}$$

Here $\boldsymbol{\xi}=(\xi_1,\ldots,\xi_m)^{\mathrm{T}}$, $\boldsymbol{F}=(F_1,\ldots,F_m)^{\mathrm{T}}$, and $F_k=\int_{\gamma}\boldsymbol{f}_k\cdot\boldsymbol{e}_3\,x_1\mathrm{d}s$ for $k=0,1,\cdots,m$.

Similarly, we have $J(u^{\mathrm{S}}) = 2\pi U^2 \mathcal{J}(\boldsymbol{\xi})$, where

$$\mathcal{J}(\boldsymbol{\xi}) := \int_\gamma \left(\boldsymbol{f}_0 + \sum_{k=1}^{m} \xi_k \boldsymbol{f}_k \right) \cdot \left(\boldsymbol{e}_3 + \sum_{j=1}^{m} \xi_j u_j^{\mathrm{S}} \boldsymbol{\tau} \right) x_1 \mathrm{d}s = \boldsymbol{\xi}^{\mathrm{T}} \boldsymbol{A} \boldsymbol{\xi} + 2\boldsymbol{\xi}^{\mathrm{T}} \boldsymbol{F} + F_0. \quad (2.12)$$

The elements of the $m \times m$ matrix $\boldsymbol{A}$ are given by $A_{kj} = \int_\gamma \boldsymbol{f}_k \cdot u_j^{\mathrm{S}} \boldsymbol{\tau}\, x_1 \mathrm{d}s$. We have used the fact that $\int_\gamma \boldsymbol{f}_0 \cdot u_k^{\mathrm{S}} \boldsymbol{\tau}\, x_1 \mathrm{d}s = \int_\gamma \boldsymbol{f}_k \cdot \boldsymbol{e}_3\, x_1 \mathrm{d}s$ for the linear term by the reciprocal theorem (Happel & Brenner 1973). We note that $\boldsymbol{A}$ is symmetric, also by the reciprocal theorem. Physically speaking, $\boldsymbol{\xi}^{\mathrm{T}} \boldsymbol{A} \boldsymbol{\xi}$ represents the scaled power loss of the swimmer being held still with its slip velocity parametrized by $\boldsymbol{\xi}$, implying that $\boldsymbol{A}$ is positive-definite.

Now, the discretized optimization problem becomes

$$\min_{\boldsymbol{\xi} \in \mathbb{R}^m} \mathcal{J}(\boldsymbol{\xi}) \quad \text{subject to } \mathcal{F}(\boldsymbol{\xi}) = 0. \quad (2.13)$$

Introducing the Lagrangian $L(\boldsymbol{\xi}, \lambda) := \mathcal{J}(\boldsymbol{\xi}) - 2\lambda \mathcal{F}(\boldsymbol{\xi})$, the slip optimization problem is reduced to solving the first-order stationarity equations for L given by

$$\begin{bmatrix} \boldsymbol{A} & -\boldsymbol{F} \\ -\boldsymbol{F}^{\mathrm{T}} & 0 \end{bmatrix} \begin{bmatrix} \boldsymbol{\xi} \\ \lambda \end{bmatrix} = \begin{bmatrix} -\boldsymbol{F} \\ F_0 \end{bmatrix}. \quad (2.14)$$

Note that forming the matrix requires $(m+1)$ solves of the forward problem (2.1) with appropriate boundary conditions. Since the micro-swimmer is assumed to be rigid, the single layer potential operator $\mathcal{S}$ as well as the traction operator $\mathcal{T}$, required for forming $\boldsymbol{A}$ and $\boldsymbol{F}$, are both fixed for a given shape. Therefore, we only need to form them once.

3. Results

We tested the convergence of our numerical solvers rigorously; validation results are presented in supplementary information (SI). Here we focus on analysis of the optimal solutions for various micro-swimmer shape families. Let V be the volume enclosed by the swimmer. We normalize lengths by the radius of a sphere of equivalent volume i.e., by $R = (3V/4\pi)^{1/3}$, and velocities by the swimming speed U. A simple calculation shows that, for a micro-swimmer submerged in water of size $R = 5\,\mu$m and the speed of one body-length per second, the Reynolds number (Re) $\approx 5 \times 10^{-5}$; thereby, confirming the validity of the Stokes equation (2.1). We will use the dimensionless *reduced volume*, defined by $\nu = 6\sqrt{\pi}V/A^{3/2}$ where A is the surface area of the given shape, to characterize each shape family. The largest possible value of ν, attained by spheres, is $\nu = 1$, while for example ν decreases monotonically for ellipsoids as the aspect-ratio is increased.

We first consider six different micro-swimmer shapes and plot their optimal slip profiles obtained by solving (2.14) in Figure 2. In each case, we also show the flow fields in both the body and lab frames. The optimal slip velocities plotted against the arclength, measured from north pole to south pole, are shown in the insets. In the case of a sphere (Fig. 2(a)), we recover the standard result that the optimal profile is a sine curve (Michelin & Lauga 2010). The optimal slip velocity of the prolate swimmer, shown in Fig. 2(b), 'flattens' the sine curve in the middle while that of the oblate swimmer, shown in Fig. 2(c), 'pinches' the sine curve. Additionally, the peak value of the optimal slip velocity is low for the prolate swimmer, and high for the oblate swimmer, compared to the spherical swimmer.

Next, we consider three shapes corresponding to different shape families—mathematical equations for all of them are provided in SI. In Fig. 2(d), we consider the 'wavy' configuration obtained by adding high-order axisymmetric modes to the spherical

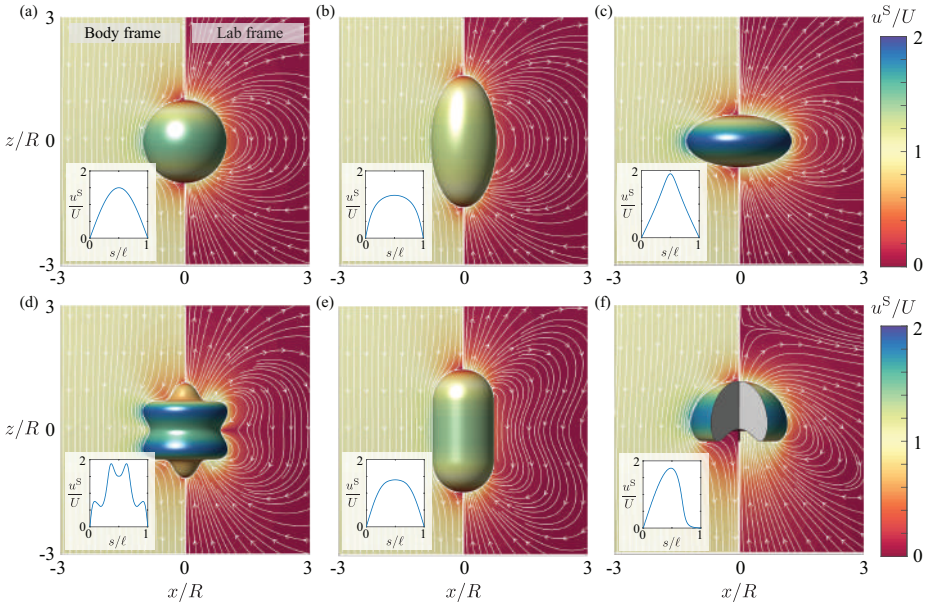

FIGURE 2. Flow fields and the optimal slip velocity for a few swimmers with typical shapes: (a) Sphere, (b) Prolate ellipsoid, (c) Oblate ellipsoid, (d) Wavy, (e) Spherocylinder, (f) Stomatocyte. Insets show the optimal slip velocities as functions of arc-length along the generating curve. The optimization is performed using 21 control points on the generating curve for representing the slip velocity.

shape. The optimal slip velocity follows the general trend for that of (a), while lower slip velocities are observed at the troughs, qualitatively consistent to those obtained in Vilfan (2012). The spherocylinder (Fig. 2(e)) resembles closely the prolate ellipsoid of Fig. 2(b) with the same aspect ratio, its optimal slip velocity being nearly the same (albeit with a slightly narrower plateau and higher peak slip velocity). Finally, we investigate the optimal slip velocity of the stomatocyte shape (Fig. 2(f)), which is the only non-convex shape among those considered here. Similar to that of the oblate swimmer, the general slip velocity is like a pinched sine wave. However, one distinguishing feature is that slip velocity is nearly zero over part of its surface, namely the cup-like region in its posterior.

We note that judging by the flow field, all optimal swimmers studied here appear to be neutral swimmers (as opposed to pushers or pullers), even though some of them (e.g., the stomatocyte) have front-back asymmetric shapes. Additionally, the optimal slip velocity is proportional to the target swimming speed U due to linearity of the Stokes equations. As a consequence, while the results only showcase micro-swimmers propelling themselves in the positive $\boldsymbol{e}_3$ direction, the optimal solution u^{S*} for swimming in the opposite direction is merely a change of sign.

Next, we study the optimal active force density $\boldsymbol{f}$ corresponding to the same shapes. Its normal and tangential components are plotted in Fig. 3. We note that by the no-net-force condition (2.5), the power loss reduces to $P = 2\pi \int_\gamma \boldsymbol{f} \cdot (u^S \boldsymbol{\tau}) x_1 \mathrm{d}s$, implying that only the tangential component contributes to the power loss. The change in tangential forces as a function of arclength loosely resembles that of the optimal slip velocity, mediated by the local curvature along the generating curve. Qualitatively, a low local curvature suppresses the traction and a high local curvature amplifies it. Slip velocities scaled by their local curvatures are shown in black dotted curves for a reference.

In Fig. 4, we plot the minimal power loss as a function of the reduced volume for

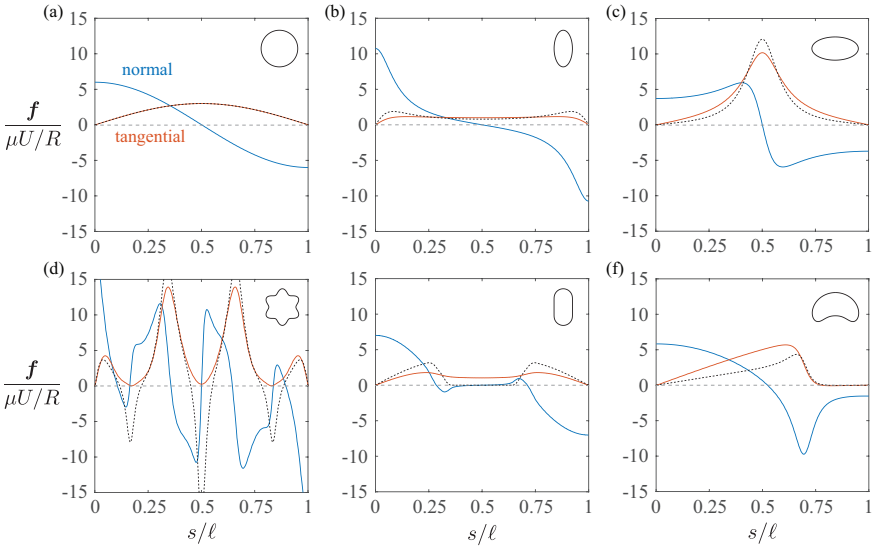

FIGURE 3. Active force density on the swimmer surface as functions of arc-length along the generating curve. Normal and tangential components of the force densities are depicted by blue and orange curves. Scaled optimal slip velocities $2u^{S*}\kappa R/U$ are shown in dotted curves, where κ is the local curvature. Insets are the shapes of the corresponding swimmers.

various shape families, scaled by that of the spherical swimmer with the same volume. The minimal power loss for prolate ellipsoids monotonically decreases as the shape gets more slender; in contrast, it is well-known that the shape with the minimal fluid drag is one with approximately 2:1 aspect ratio (Pironneau 1973). By slender body theory, the power loss of a prolate ellipsoid scales as $\sim \mu\alpha^{2/3}U^2$, where α is the aspect ratio (see Leshansky *et al.* (2007)). On the other hand, the minimal power loss for oblate ellipsoids grows rapidly as the reduced volume is increased. Shapes of the spherocylinder family behave similarly to the prolate ellipsoids, and converge to the spherical case when the length of the cylinder reduces to 0, as expected. It is however worth pointing out that spherocylinder costs more power loss than prolate ellipsoids with the same reduced volume; this relates to the fact that the peak slip velocity for spherocylinder is higher than that of the prolate ellipsoid (Fig. 2 (b)&(e)). The stomatocyte family is constructed by 'pulling' the rim of the shape, effectively making the shape 'taller' and curls deeper and deeper inside. We find that 'taller' shapes requires lower power loss for this shape family, which is qualitatively consistent with the ellipsoid family. Finally, we note that the power loss of the snowman family (two spheres attaching with each other) is quite robust to the relative sizes of the two spheres. The power loss is only about 25% higher than that of a single sphere in the limit case where the two spheres are of the same size.

A few other examples that take more generic shapes are also shown in Figure 4. The optimal slip velocities are colored on their surfaces while their power loss is shown in the form of scatter points. The generating curve of these shapes are formed by spherical harmonics. We note that the optimal performance of shapes that appear similar can be very different. For example, the difference in power loss between examples 6 and 8 is about 150% of the spherical swimmer, or 60% of example 6. This result is a strong indicator that the slip velocity of the artificial swimmer, as well as its shape, must be carefully designed to achieve good performance.

We note that the minimal power loss for all the shape familites considered here are

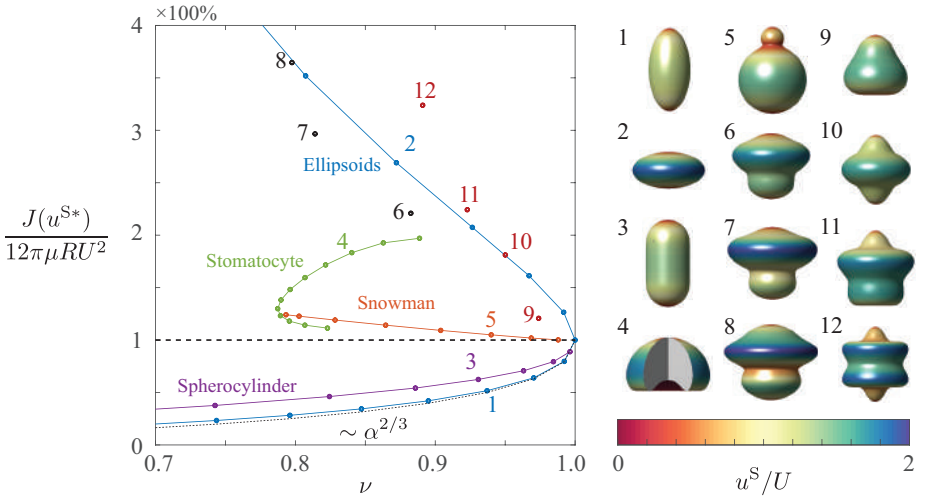

FIGURE 4. Scaled minimal power loss of different shape families, plotted against the reduced volume ν. Example shapes are color-coded by the optimal slip velocity. The dotted line shows the theoretical limit of power loss given by the slender body theory (Leshansky *et al.* 2007).

bounded from below by the curve for prolate ellipsoids, agreeing with the analysis made by Leshansky *et al.* (2007).

4. Conclusions

In this work, we provided a solution procedure for the PDE-constrained optimization problem of finding the optimal slip profile on an axisymmetric micro-swimmer that minimizes the power loss required to maintain a target swimming speed. While it can be extended to other objective functions, we exploited the quadratic nature of the power loss functional in the control parameters to simplify and streamline the solution procedure. In the general case, an adjoint formulation and iterative optimization algorithms can be employed. Regardless of the formulation, however, the use of boundary integral method to solve the Stokes equations greatly reduces the computational cost due to dimensionality reduction. Solving any of the examples presented in this work, for example, required only a few seconds on a standard laptop. Extending our procedure to fully three-dimensional (non-axisymmetric) shapes is straightforward; the key technical challenge is incorporating a high-order boundary integral solver, for which open-source codes are now available (e.g., see Gimbutas & Veerapaneni (2013)).

The optimal slip velocities of different families of bio-relevant shapes and common phoretic particle shapes were studied and compared against idealized shapes. We found that optimal slip velocity for all shapes, even with front-back asymmetric shapes, could be viewed as neutral swimmers. This mirrors the findings in Stone & Samuel (1996) that swimmers that create no vorticity in the surrounding fluid spend less energy than those which do. Additionally, the power loss of micro-swimmers seem to be bounded from below by prolate ellipsoids with the same reduced volume.

The optimization procedure developed in this work can directly be employed in the design pipeline of autophoretic particles. For example, in the case of diffusiophoresis, the computed optimal slip profile for a given shape can be used to formulate the chemical coating pattern of the phoretic particles. Another natural extension of this work is to relax the steady slip assumption and consider time-periodic squirming motion as done

in Michelin & Lauga (2010). This would be particularly useful for studying the ciliary locomotion of micro-organisms with arbitrary shapes. Furthermore, building on the recent work of Bonnet *et al.* (2020), we are developing solvers for the shape optimization problem of finding the most efficient microswimmer shapes under specified area, volume or other physical constraints.

Authors gratefully acknowledge support from NSF under grants DMS-1719834 and DMS-1454010.

REFERENCES

Anderson, J. L. 1989 Colloid transport by interfacial forces. *Annual review of fluid mechanics* **21** (1), 61–99.

Aubret, A. & Palacci, J. 2018 Diffusiophoretic design of self-spinning microgears from colloidal microswimmers. *Soft matter* **14** (47), 9577–9588.

Blake, J. R. 1971 A spherical envelope approach to ciliary propulsion. *Journal of Fluid Mechanics* **46** (01), 199–208.

Bonnet, M., Liu, R. & Veerapaneni, S. 2020 Shape optimization of stokesian peristaltic pumps using boundary integral methods. *Advances in Computational Mathematics* **46** (2), 1–24.

Choudhury, U., Straube, A. V., Fischer, P., Gibbs, J. G. & Höfling, F. 2017 Active colloidal propulsion over a crystalline surface. *New Journal of Physics* **19** (12), 125010.

Gimbutas, Z. & Veerapaneni, S. 2013 A fast algorithm for spherical grid rotations and its application to singular quadrature. *SIAM Journal on Scientific Computing* **35** (6), A2738–A2751.

Golestanian, R., Liverpool, T. B. & Ajdari, A. 2007 Designing phoretic micro-and nano-swimmers. *New Journal of Physics* **9** (5), 126.

Happel, J. & Brenner, H. 1973 *Low Reynolds number hydrodynamics with special applications to particulate media*. Noordhoff.

Howse, J. R., Jones, R. A., Ryan, A. J., Gough, T., Vafabakhsh, R. & Golestanian, R. 2007 Self-motile colloidal particles: from directed propulsion to random walk. *Physical review letters* **99** (4), 048102.

Kyoya, K., Matsunaga, D., Imai, Y., Omori, T. & Ishikawa, T. 2015 Shape matters: Near-field fluid mechanics dominate the collective motions of ellipsoidal squirmers. *Physical Review E* **92** (6), 063027.

Lauga, E. & Powers, T. R. 2009 The hydrodynamics of swimming microorganisms. *Reports on Progress in Physics* **72** (9), 096601.

Leshansky, A. M., Kenneth, O., Gat, O. & Avron, J. E. 2007 A frictionless microswimmer. *New Journal of Physics* **9** (5), 145.

Lighthill, J. 1952 On the squirming motion of nearly spherical deformable bodies through liquids at very small reynolds numbers. *Communications on Pure and Applied Mathematics* **5** (2), 109–118.

Lighthill, S. J. 1975 *Mathematical biofluiddynamics*. SIAM.

Lynn, D. 2008 *The ciliated protozoa: characterization, classification, and guide to the literature*. Springer Science & Business Media.

Michelin, S. & Lauga, E. 2010 Efficiency optimization and symmetry-breaking in a model of ciliary locomotion. *Physics of Fluids* **22** (11), 111901.

Morgan, A. R., Dawson, A. B., Mckenzie, H. S., Skelhon, T. S., Beanland, R., Franks, H. P. & Bon, S. A. 2014 Chemotaxis of catalytic silica–manganese oxide 'matchstick' particles. *Materials Horizons* **1** (1), 65–68.

Palacci, J., Sacanna, S., Abramian, A., Barral, J., Hanson, K., Grosberg, A. Y., Pine, D. J. & Chaikin, P. M. 2015 Artificial rheotaxis. *Science advances* **1** (4), e1400214.

Paxton, W. F., Kistler, K. C., Olmeda, C. C., Sen, A., St. Angelo, S. K., Cao, Y., Mallouk, T. E., Lammert, P. E. & Crespi, V. H. 2004 Catalytic nanomotors: autonomous movement of striped nanorods. *Journal of the American Chemical Society* **126** (41), 13424–13431.

Pedley, T. J. 2016 Spherical squirmers: models for swimming micro-organisms. *IMA Journal of Applied Mathematics* **81** (3), 488–521.

Pironneau, O. 1973 On optimum profiles in stokes flow. *Journal of Fluid Mechanics* **59** (1), 117–128.

Pozrikidis, C. 1992 *Boundary integral and singularity methods for linearized viscous flow*. Cambridge University Press.

Simmchen, J., Baeza, A., Miguel-Lopez, A., Stanton, M. M., Vallet-Regi, M., Ruiz-Molina, D. & Sánchez, S. 2017 Dynamics of novel photoactive agcl microstars and their environmental applications. *ChemNanoMat* **3** (1), 65–71.

Stone, H. A. & Samuel, A. D. 1996 Propulsion of microorganisms by surface distortions. *Physical review letters* **77** (19), 4102.

Uspal, W. E., Popescu, M. N., Tasinkevych, M. & Dietrich, S. 2018 Shape-dependent guidance of active janus particles by chemically patterned surfaces. *New Journal of Physics* **20** (1), 015013.

Valadares, L. F., Tao, Y.-G., Zacharia, N. S., Kitaev, V., Galembeck, F., Kapral, R. & Ozin, G. A. 2010 Catalytic nanomotors: Self-propelled sphere dimers. *Small* **6** (4), 565–572.

Veerapaneni, S. K., Gueyffier, D., Biros, G. & Zorin, D. 2009 A numerical method for simulating the dynamics of 3d axisymmetric vesicles suspended in viscous flows. *Journal of Computational Physics* **228** (19), 7233–7249.

Vilfan, A. 2012 Optimal shapes of surface slip driven self-propelled microswimmers. *Physical review letters* **109** (12), 128105.

Optimal slip velocities of micro-swimmers with arbitrary axisymmetric shapes: Supplemental material

Hanliang Guo[1], Hai Zhu[1], Ruowen Liu[1], Marc Bonnet[2], and Shravan Veerapaneni[1]†

[1]Department of Mathematics, University of Michigan, Ann Arbor, MI, 48109 USA.
[2]POEMS (CNRS, INRIA, ENSTA), ENSTA, 91120 Palaiseau, France.

(Received xx; revised xx; accepted xx)

1. Parameter space

We parametrize the slip velocity by a B-spline formulation. Simply speaking, the slip velocity $u^{\mathrm{S}}(t)$ is determined by $(M+1)$ *control points*, $u^{\mathrm{S}}(t_i) = \varphi_i$ for $i = 0, \cdots, M$, and is interpolated by B-spline basis functions between the control points. Here $t \in [0, \pi]$ is a reparametrization of the arc-length s. In theory, we only need to assign control points for t_i between 0 and π to generate an admissible slip velocity by symmetry. In practice, however, we assign control points in the full period $t_i \in [0, 2\pi]$ and impose periodic boundary conditions to determine the spline coefficients, as detailed below.

Let $M = 2N + 2$, where N is the number of *free* control points between 0 and π. Let all control points be equally spaced, we have $t_i = 2\pi i/M$, $i = 0, \cdots, M$. To make sure the slip velocity is axisymmetric, we assign *ghost* control points $\varphi_i = -\varphi_{M-i}$ for $N+1 < i < 2N+2$ and enforce zero conditions at the poles $\varphi_i = 0$, for $i = 0, N+1, 2N+2$.

The general B-spline formulation of order 5 is given by

$$u^{\mathrm{S}}(t) := \sum_{k=-5}^{M-1} \xi_k B_k(t), \quad t \in [0, 2\pi], \tag{1.1}$$

where $B_k(t) = B^*_{k,5}(\frac{M}{2\pi}t)$ is a modified k-th B-spline basis function, and $B^*_{k,p}$ is the standard k-th B-spline basis function of degree p, given by recurrence

$$B^*_{k,0}(t) = \begin{cases} 1, & k \leqslant t < k+1 \\ 0, & \text{otherwise} \end{cases} \tag{1.2}$$

$$B^*_{k,p}(t) = \frac{t-k}{p} B^*_{k,p-1}(t) + \frac{p+k+1-t}{p} B^*_{k+1,p-1}(t). \tag{1.3}$$

In order to obtain the $(M+5)$ B-spline coefficients ξ_k from the $(M+1)$ control points φ_i, we need four more equations to close the system. Specifically, we use the periodic boundary conditions of the derivatives

$$\frac{\mathrm{d}^n u^{\mathrm{S}}}{\mathrm{d}t^n}(0) = \frac{\mathrm{d}^n u^{\mathrm{S}}}{\mathrm{d}t^n}(2\pi), \quad n = 1, 2, 3, 4. \tag{1.4}$$

These system of equations uniquely determine the B-spline coefficient ξ_k from the control points φ_i. The slip velocity $u^{\mathrm{S}}(t)$ along the generating curve could then be found by substituting ξ_k into (1.1).

† Email address for correspondence: shravan@umich.edu

2. Numerical validation

To validate our boundary integral method, we construct a boundary value problem and test the algorithm against the exact solution. The exact flow field generated by axisymmetric stokeslets and the resulted traction on the surface can be computed analytically by

$$\boldsymbol{u}_{exa}(\boldsymbol{x}) = \sum_{k=1}^{N} K(\boldsymbol{x},k)\boldsymbol{\mu}_{exa}(k)y_1(k), \quad \boldsymbol{f}_{exa}(\gamma) = \sum_{k=1}^{N} T(\gamma,k)\boldsymbol{\mu}_{exa}(k)y_1(k), \tag{2.1}$$

where $\{\boldsymbol{y}(k)\}$ and $\{\boldsymbol{\mu}_{exa}(k)\}$ are the location and strength of the k-th stokeslet, $K(\boldsymbol{x},s)$ is a kernel composed of elliptic integrals of first and second kind (Veerapaneni *et al.* 2009) and

$$T(\boldsymbol{x},s) = \int_0^{2\pi} dv \begin{bmatrix} \frac{(y_1(s)\cos(v)-x_1)(y_1(s)-x_1\cos(v))}{|r^5|} & \frac{(y_1(s)\cos(v)-x_1)(y_2(s)-x_2)}{|r^5|} \\ \frac{(y_1(s)-x_1\cos(v))(y_2(s)-x_2)}{|r^5|} & \frac{(y_2(s)-x_2)^2}{|r^5|} \end{bmatrix} \cdot \\ (n_1\left(y_1\left(s\right)\cos\left(v\right)-x_1\right)+n_2\left(y_2\left(s\right)-x_2\right)), \quad \boldsymbol{x}\in\gamma. \tag{2.2}$$

We randomly choose 5 stokeslet whose locations and strengths are given in Figure 1(a) by the black arrows and substitute them into (2.1) as our reference case.

To obtain the numerical solution, we first evaluate the reference flow field on the generating curve $\boldsymbol{u}_{exa}(\gamma)$, then treat $\boldsymbol{u}_{exa}(\gamma)$ as the boundary condition to obtain the density vector $\boldsymbol{\mu}$ from $\mathcal{S}[\boldsymbol{\mu}](\gamma) = \boldsymbol{u}_{exa}(\gamma)$. We subsequently use the density vector $\boldsymbol{\mu}$ to evaluate the flow field $\boldsymbol{u}_{num}(\boldsymbol{x})$ outside the micro-swimmer's surface. The traction on the generating curve is evaluated from the same density vector $\boldsymbol{\mu}$ using the traction kernel $\boldsymbol{f}_{num}(\gamma) = (-\frac{1}{2}\mathcal{I}+\mathcal{T})[\boldsymbol{\mu}](\gamma) = -\frac{1}{2}\boldsymbol{\mu}(\gamma) + \int_\gamma T(\boldsymbol{x},s)\boldsymbol{\mu}(s)y_1(s)ds_{\boldsymbol{y}}$.

In the case of axisymmetric flow for a single micro-swimmer suspended in an unbounded viscous fluid, we adapt a single layer potential formulation used in Veerapaneni *et al.* (2009). The logarithm of absolute error between $\boldsymbol{u}_{exa}$ and $\boldsymbol{u}_{num}$ is shown in figure 1(a) with 400 Gauss-Legendre quadrature points on γ. The numerical method of the forward problem has a 10-digits spatial accuracy for flow field and 6-digits spatial accuracy for traction with 400 quadrature points on the generating curve, as shown in figure 1(b) &(c). In all of our simulations, 600 Gauss-Legendre quadrature points are used.

By way of validation, we also computed the fluid drag of a family of prolate and oblate ellipsoids. The shape that yields the minimal fluid drag is a prolate ellipsoid with a roughly $2:1$ aspect ratio (Fig. 2), consistent with the optimal shape obtained previously in Pironneau (1973).

3. Generating curves of the shapes used in the paper

Some of the generating curves used in the paper can be easily expressed as functions of imaginary variables. In all cases below, $i=\sqrt{-1}$, $t\in[0,\pi]$ is the polar angle. The axis of symmetry is the imaginary axis.

(i)Ellipsoids: $z=\alpha^{-1/3}\sin(t)+i\alpha^{2/3}\cos(t)$, α is the aspect ratio.

(ii)Wavy shapes: $z=(1+0.15\cos(kt)\exp(i(\pi/2-t)))$, $k\in\{3,4,5,6\}$ is the order of the perturbation.

(iii)Stomatocyte: $z=(1.5+\cos t)(\sin(\lambda\pi\sin t)+i\cos(\lambda\pi\sin t))-0.5i$, $\lambda\in[0.4,0.95]$ measures the vertical 'stretchness' of the shape.

(iv)Harmonics: $z=\rho(t)\sin t - i\rho(t)\cos t$, where $\rho(t)=1+rY_n^m(t,0)$, where $Y_n^m(\theta,\varphi)$ is the

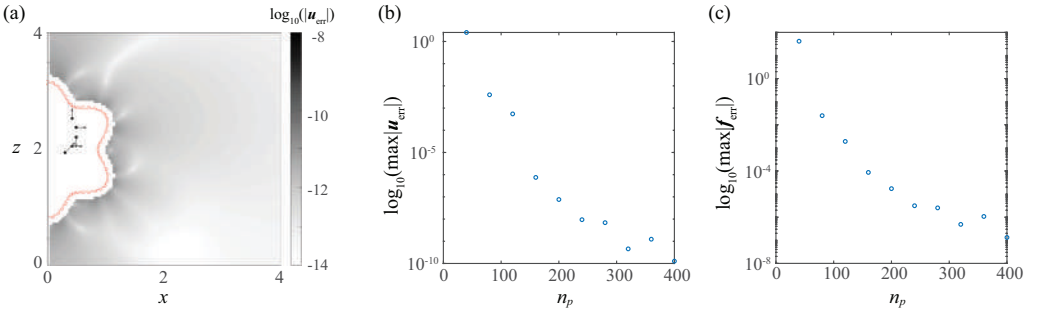

FIGURE 1. (a) The absolute error between the exact solution and the numerical solution with a total of 400 Gaussian quadrature points, color-code represents $\log_{10}(|\boldsymbol{u}_{exa} - \boldsymbol{u}_{num}|)$. (b) The L_∞-norm of the flow field shown as a function of the number of quadrature points. (c) The L_∞-norm of the traction on the surface shown as a function of the number of quadrature points.

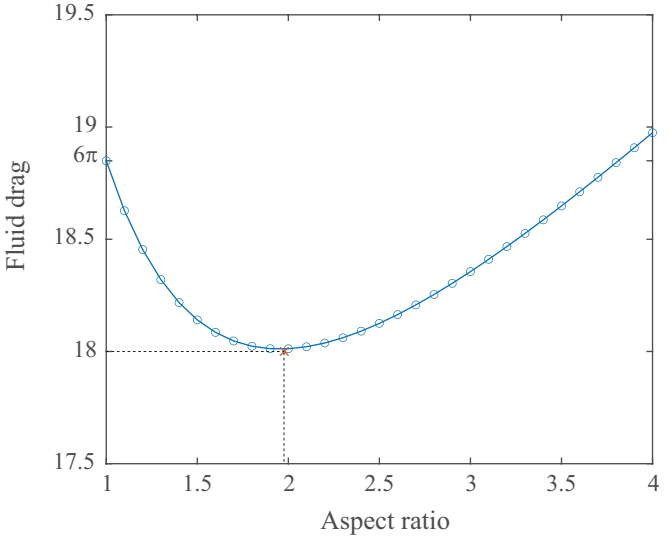

FIGURE 2. Fluid drag of towing a prolate ellipsoid with unit speed. All ellipsoids are of the same volume as the unit sphere. The red cross denotes the fluid drag of the optimal profile that minimizes the fluid drag given by Pironneau (1973).

spherical harmonics of degree n and order m, evaluated at the colatitude θ and longitude φ.

On the other hand, the spherocylinder shapes consists of two semi-spherical caps and a cylinder with the same radius; the snowman shapes consists of two spheres of different radii glued together with the centroid distance being 90% of the sum of the radii. These shapes are smoothed by B-spline interpolations of order 5.

REFERENCES

PIRONNEAU, OLIVIER 1973 On optimum profiles in stokes flow. *Journal of Fluid Mechanics* **59** (1), 117–128.

VEERAPANENI, SHRAVAN K, GUEYFFIER, DENIS, BIROS, GEORGE & ZORIN, DENIS 2009 A numerical method for simulating the dynamics of 3d axisymmetric vesicles suspended in viscous flows. *Journal of Computational Physics* **228** (19), 7233–7249.